Computational and Applied Mathematics Journal
2015; 1(4): 186-200
Published online July 10, 2015 (http://www.aascit.org/journal/camj)

American Association for Science and Technology

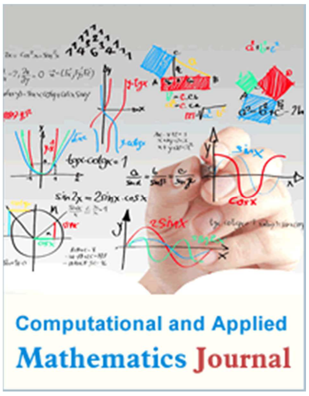

Keywords
Granville Turbulence Model,
Coakley Turbulence Model,
Wilcox Turbulence Model,
Baldwin and Barth Turbulence Model,
Navier-Stokes Equations,
Three-Dimensions

Received: June 3, 2015
Revised: June 16, 2015
Accepted: June 17, 2015

Assessment of Several Turbulence Models Applied to Supersonic Flows in Three-Dimensions – Part II

Edisson S. G. Maciel

Aeronautical Engineering Division (IEA), Aeronautical Technological Institute (ITA), SP, Brasil

Email address
edisavio@edissonsavio.eng.br

Citation
Edisson S. G. Maciel. Assessment of Several Turbulence Models Applied to Supersonic Flows in Three-Dimensions – Part II. *Computational and Applied Mathematics Journal.*
Vol. 1, No. 4, 2015, pp. 186-200.

Abstract
In the present work, the Van Leer and the Liou and Steffen Jr. flux vector splitting schemes are implemented to solve the three-dimensional Favre-averaged Navier-Stokes equations. The Granville algebraic model, the Coakley and the Wilcox two-equation models, and the Baldwin and Barth one-equation model are used in order to close the problem. The physical problem under study is the supersonic flow around a blunt body configuration. The results have demonstrated that the Van Leer scheme using the Granville turbulence model has yielded the best value of the stagnation pressure at the blunt body nose.

1. Introduction

Conventional non-upwind algorithms have been used extensively to solve a wide variety of problems ([1]). Conventional algorithms are somewhat unreliable in the sense that for every different problem (and sometimes, every different case in the same class of problems) artificial dissipation terms must be specially tuned and judicially chosen for convergence. Also, complex problems with shocks and steep compression and expansion gradients may defy solution altogether.

Upwind schemes are in general more robust but are also more involved in their derivation and application. Some upwind schemes that have been applied to the Euler equations are: [2-3]. A description of these methods is found in [4].

In relation to turbulent flow simulations, [5] applied the Navier-Stokes equations to transonic flows problems along a convergent-divergent nozzle and around the NACA 0012 airfoil. The [6] model was used to close the problem. Three algorithms were implemented: the [7] explicit scheme, the [8] implicit scheme and the [9] explicit scheme. The results have shown that, in general terms, the [7] and the [9] schemes have presented better solutions.

For a more detailed description of the motivation of the present study, as well some comments about different turbulence models the reader is encouraged to read [4].

In the present work, the [2-3] flux vector splitting schemes are implemented, on a finite-volume context. The three-dimensional Favre-averaged Navier-Stokes equations are solved using an upwind discretization on a structured mesh. The [10] algebraic model, the [11] and [12] $k^{1/2}$-ω and k-ω two-equation models, respectively, and the [13] one-equation model are used in order to close the problem. The physical problem under study is the supersonic flow around a blunt body configuration. The implemented schemes are first-order accurate in space. The time integration uses a Runge-Kutta method of five stages and is second-order accurate. The algorithms are accelerated to the steady state solution using a spatially variable time step. This technique has proved excellent gains in terms of convergence rate as reported in [14-15]. The results have demonstrated that the

[2] scheme using the [10] turbulence model has yielded the best value of the stagnation pressure at the blunt body nose.

2. Three-Dimensional Navier-Stokes Equations

The three-dimensional flow is modeled by the Navier-Stokes equations, which express the conservation of mass and energy as well as the momentum variation of a viscous, heat conducting and compressible media, in the absence of external forces. The Navier-Stokes equations are presented in their two-equation turbulence model formulation. For the algebraic model, these two-equations are neglected and the [2-3] algorithms are applied only to the original five conservation equations. The one-equation model considers only one additional equation. The integral form of these equations may be represented by:

$$\partial/\partial t\int_V Q dV+\int_S\left[\left(E_e-E_v\right)n_x+\left(F_e-F_v\right)n_y+\left(G_e-G_v\right)n_z\right]dS+\int_V M dV=0\,, \tag{1}$$

where Q is written for a Cartesian system, V is the cell volume, n_x, n_y, and n_z are components of the unity vector normal to the cell boundary, S is the flux area, E_e, F_e and G_e are the components of the convective, or Euler, flux vector, E_v, F_v and G_v are the components of the viscous, or diffusive, flux vector and M is the source term of the two-equation models. The vectors Q, E_e, F_e, G_e, E_v, F_v and G_v are, incorporating a k-s formulation, represented by:

$$Q=\begin{Bmatrix}\rho\\ \rho u\\ \rho v\\ \rho w\\ e\\ \rho k\\ \rho s\end{Bmatrix},\ E_e=\begin{Bmatrix}\rho u\\ \rho u^2+p\\ \rho uv\\ \rho uw\\ (e+p)u\\ \rho ku\\ \rho su\end{Bmatrix},\ F_e=\begin{Bmatrix}\rho v\\ \rho vu\\ \rho v^2+p\\ \rho vw\\ (e+p)v\\ \rho kv\\ \rho sv\end{Bmatrix},\ G_e=\begin{Bmatrix}\rho w\\ \rho wu\\ \rho wv\\ \rho w^2+p\\ (e+p)w\\ \rho kw\\ \rho sw\end{Bmatrix}; \tag{2}$$

$$E_v=\begin{Bmatrix}0\\ t_{xx}+\tau_{xx}\\ t_{xy}+\tau_{xy}\\ t_{xz}+\tau_{xz}\\ f_x\\ \alpha_x\\ \beta_x\end{Bmatrix},\ F_v=\begin{Bmatrix}0\\ t_{xy}+\tau_{xy}\\ t_{yy}+\tau_{yy}\\ t_{yz}+\tau_{yz}\\ f_y\\ \alpha_y\\ \beta_y\end{Bmatrix},\ G_v=\begin{Bmatrix}0\\ t_{xz}+\tau_{xz}\\ t_{yz}+\tau_{yz}\\ t_{zz}+\tau_{zz}\\ f_z\\ \alpha_z\\ \beta_z\end{Bmatrix}; \tag{3}$$

$$M=\{0\quad 0\quad 0\quad 0\quad 0\quad M_k\quad M_s\}^T, \tag{4}$$

where the components of the viscous stress tensor are defined as:

$$\begin{aligned}
t_{xx}&=\left[2\mu_M\,\partial u/\partial x-2/3\mu_M\left(\partial u/\partial x+\partial v/\partial y+\partial w/\partial z\right)\right]/Re;\\
t_{xy}&=\mu_M\left(\partial u/\partial y+\partial v/\partial x\right)/Re;\\
t_{xz}&=\mu_M\left(\partial u/\partial z+\partial w/\partial x\right)/Re;\\
t_{yy}&=\left[2\mu_M\left(\partial v/\partial y\right)-2/3\mu_M\left(\partial u/\partial x+\partial v/\partial y+\partial w/\partial z\right)\right]/Re;\\
t_{yz}&=\mu_M\left(\partial v/\partial z+\partial w/\partial y\right)/Re;\\
t_{zz}&=\left[2\mu_M\left(\partial w/\partial z\right)-2/3\mu_M\left(\partial u/\partial x+\partial v/\partial y+\partial w/\partial z\right)\right]/Re.
\end{aligned} \tag{5}$$

The components of the turbulent stress tensor (Reynolds stress tensor) are described by the following expressions:

$$\begin{aligned}
\tau_{xx}&=\left[2\mu_T\,\partial u/\partial x-2/3\mu_T\left(\partial u/\partial x+\partial v/\partial y+\partial w/\partial z\right)\right]/Re\ -2/3\rho k;\\
\tau_{xy}&=\mu_T\left(\partial u/\partial y+\partial v/\partial x\right)/Re;\\
\tau_{xz}&=\mu_T\left(\partial u/\partial z+\partial w/\partial x\right)/Re;\\
\tau_{yy}&=\left[2\mu_T\left(\partial v/\partial y\right)-2/3\mu_T\left(\partial u/\partial x+\partial v/\partial y+\partial w/\partial z\right)\right]/Re-2/3\rho k;\\
\tau_{yz}&=\mu_T\left(\partial v/\partial z+\partial w/\partial y\right)/Re;\\
\tau_{zz}&=\left[2\mu_T\left(\partial w/\partial z\right)-2/3\mu_T\left(\partial u/\partial x+\partial v/\partial y+\partial w/\partial z\right)\right]/Re-2/3\rho k.
\end{aligned} \tag{6}$$

Expressions to f_x, f_y and f_z are given bellow:

$$\begin{aligned}
f_x&=\left(t_{xx}+\tau_{xx}\right)u+\left(t_{xy}+\tau_{xy}\right)v+\left(t_{xz}+\tau_{xz}\right)w-q_x;\\
f_y&=\left(t_{xy}+\tau_{xy}\right)u+\left(t_{yy}+\tau_{yy}\right)v+\left(t_{yz}+\tau_{yz}\right)w-q_y;\\
f_z&=\left(t_{xz}+\tau_{xz}\right)u+\left(t_{yz}+\tau_{yz}\right)v+\left(t_{zz}+\tau_{zz}\right)w-q_z,
\end{aligned} \tag{7}$$

where q_x, q_y and q_z are the Fourier heat flux components and are given by:

$$\begin{aligned}
q_x&=-\gamma/Re\left(\mu_M/Pr_L+\mu_T/Pr_T\right)\partial e_i/\partial x;\\
q_y&=-\gamma/Re\left(\mu_M/Pr_L+\mu_T/Pr_T\right)\partial e_i/\partial y;\\
q_z&=-\gamma/Re\left(\mu_M/Pr_L+\mu_T/Pr_T\right)\partial e_i/\partial z.
\end{aligned} \tag{8}$$

The diffusion terms related to the k-s equations are defined as:

$$\begin{aligned}
\alpha_x&=1/Re\left(\mu_M+\mu_T/\sigma_k\right)\partial k/\partial x;\\
\alpha_y&=1/Re\left(\mu_M+\mu_T/\sigma_k\right)\partial k/\partial y;\\
\alpha_z&=1/Re\left(\mu_M+\mu_T/\sigma_k\right)\partial k/\partial z;
\end{aligned} \tag{9}$$

$$\begin{aligned}
\beta_x&=1/Re\left(\mu_M+\mu_T/\sigma_s\right)\partial s/\partial x;\\
\beta_y&=1/Re\left(\mu_M+\mu_T/\sigma_s\right)\partial s/\partial y;\\
\beta_z&=1/Re\left(\mu_M+\mu_T/\sigma_s\right)\partial s/\partial z.
\end{aligned} \tag{10}$$

In the above equations, ρ is the fluid density; u, v and w are Cartesian components of the velocity vector in the x, y and z directions, respectively; e is the total energy per unit volume; p is the static pressure; k is the turbulence kinetic energy; s is the second turbulent variable, which is the vorticity ($k^{1/2}$-ω or k-ω models) for this work; the t's are viscous stress components; τ's are the Reynolds stress components; the q's are the Fourier heat flux components; M_k takes into account the production and the dissipation terms of k; M_s takes into account the production and the dissipation terms of s; μ_M and μ_T are the molecular and the turbulent viscosities, respectively; Pr_L and Pr_T are the laminar and the turbulent Prandtl numbers, respectively; σ_k and σ_s are turbulence coefficients; γ is the ratio of specific heats; Re is the viscous Reynolds number, defined by:

$$\mathrm{Re} = \rho V_{REF} l_{REF} / \mu_M \,, \tag{11}$$

where V_{REF} is a characteristic flow velocity and l_{REF} is a configuration characteristic length. The internal energy of the fluid, e_i, is defined as:

$$e_i = e/\rho - 0.5\left(u^2 + v^2 + w^2\right). \tag{12}$$

The molecular viscosity is estimated by the empiric Sutherland formula:

$$\mu_M = bT^{1/2} / \left(1 + S/T\right), \tag{13}$$

where T is the absolute temperature (K), b = 1.458x10^{-6} Kg/(m.s.K$^{1/2}$) and S = 110.4 K, to the atmospheric air in the standard atmospheric conditions ([16]).

The Navier-Stokes equations are dimensionless in relation to the freestream density, ρ_∞, the freestream speed of sound, a_∞, and the freestream molecular viscosity, μ_∞. The system is closed by the state equation for a perfect gas:

$$p = (\gamma - 1)\left[e - 0.5\rho\left(u^2 + v^2 + w^2\right) - \rho k\right], \tag{14}$$

considering the ideal gas hypothesis. The total enthalpy is given by $H = (e + p)/\rho$.

The [2-3] flux vector splitting algorithms are described in detail in [4] and the interested reader is encouraged to read this work. The viscous implementation is also described in [4]. The three-dimensional configuration like: computational cell, flux surface areas, normal vectors and cell volume are described in [17]. The spatially variable time step is described in [4; 18] and the interested reader can found in these references the detailed implementation.

3. Turbulence Models

3.1. Granville Turbulence Model

The problem of the turbulent simulation is in the calculation of the Reynolds stress. Expressions involving velocity fluctuations, originating from the average process, represent six new unknowns. However, the number of equations keeps the same and the system is not closed. The modeling function is to develop approximations to these correlations. To the calculation of the turbulent viscosity according to the [10] model, the boundary layer is divided in internal and external.

Initially, the (ν_w) kinematic viscosity at wall and the ($t_{xy,w}$ and $t_{xz,w}$) shear stresses at wall are calculated. After that, the (δ) boundary layer thickness is calculated. So, the (N) normal distance from the wall to the studied cell is calculated. The N^+ term is obtained from:

$$N^+ = \sqrt{\mathrm{Re}}\, u_T N / \nu_w \,, \tag{15}$$

where ν_w is the wall cinematic viscosity and u_T is the friction velocity, defined as:

$$u_T = \sqrt{t_{wall}}\,,\ t_{wall} = t_T / \rho_w \ \text{ and } \ t_T = \sqrt{\left(t_{xy,w}\right)^2 + \left(t_{xz,w}\right)^2}\,. \tag{16}$$

The van Driest damping factor is calculated by:

$$D = 1 - e^{\left(-N^+/A_G\right)}, \tag{17}$$

where:

$$A_G = 26 \Big/ \sqrt{1 + b\left|p^+\right|} \ \text{ and } \ p^+ = \frac{1}{\mathrm{Re}}\left[\nu_M / \left(\rho u_T^3\right)\right]\frac{dp}{dx}; \tag{18}$$

$$b = 12.6 \quad \text{if } p^+ \geq 0.0;\ b = 14.76 \quad \text{if } p^+ < 0.0\,.$$

Defining now the dimensionless coordinates ξ and η, one has:

$$\xi = \frac{\delta_{BL}}{\left|t_w \rho_w\right|}\frac{dp}{dx}\frac{1}{\mathrm{Re}} \quad \text{and} \quad \eta = \frac{N}{\delta_{BL}}. \tag{19}$$

The ratio of tangential stress is given by:

$$\frac{t}{t_T} = 1 + \xi\eta - (3 + 2\xi)\eta^2 + (2 + \xi)\eta^3. \tag{20}$$

The characteristic length is defined by

$$l_{mix} = \kappa N \sqrt{\frac{t}{t_T}} D\,. \tag{21}$$

Hence, for the internal layer, one has:

$$\mu_{Ti} = \mathrm{Re}\,\rho l_{mix}^2 \left\|\omega\right\|, \tag{22}$$

where $\|\omega\|$ is the magnitude of the vortex vector, defined as:

$$\left\|\omega\right\| = \sqrt{\left(\frac{\partial v}{\partial z} - \frac{\partial w}{\partial y}\right)^2 + \left(\frac{\partial w}{\partial x} - \frac{\partial u}{\partial z}\right)^2 + \left(\frac{\partial u}{\partial y} - \frac{\partial v}{\partial x}\right)^2}\,. \tag{23}$$

In the external layer,

$$\mu_{Te} = \mathrm{Re}\,\rho\alpha C_{cp} F_{wake} F_{Kleb}\left(N; N_{max}/C_{Kleb}\right), \tag{24}$$

with:

$$F_{wake} = \mathrm{MIN}\left[N_{max}F_{max};\ C_{wk}N_{max}U_{dif}^2 / F_{max}\right],$$
$$F_{max} = 1/\kappa\left[\underset{N}{\mathrm{MAX}}\left(l_{mix}\left\|\omega\right\|D\right)\right]; \tag{25}$$

$$C_{Kleb} = 2/3 - 0.01312 / \left(0.1724 + \bar{\beta}\right); \tag{26}$$

$$\bar{\beta} = -\frac{N_{max}}{u_T}\frac{du}{dx}\frac{1}{Re}; \tag{27}$$

$$C_{cp} = \left(3 - 4C_{Kleb}\right) / \left[2C_{Kleb}\left(2 - 3C_{Kleb}^4\right)\right]. \tag{28}$$

Hence, N_{max} is the value of N where $l_{mix}\|\omega\|D$ reached its maximum value and l_{mix} is the Prandtl mixture length. The constant values are: $\kappa = 0.4$, $\alpha = 0.0168$, and $C_{wk} = 0.25$. F_{Kleb} is the intermittent function of Klebanoff given by:

$$F_{Kleb}(N) = \left[1 + 5.5\left(C_{Kleb}N/N_{max}\right)^6\right]^{-1}, \tag{29}$$

and U_{dif} is the maximum velocity value in the boundary layer case. To free shear layers,

$$U_{dif} = \left(\sqrt{u^2 + v^2 + w^2}\right)_{max} - \left(\sqrt{u^2 + v^2 + w^2}\right)_{N=N_{max}}. \tag{30}$$

Finally, the turbulent viscosity is chosen from the internal and the external viscosities: $\mu_T = MIN(\mu_{Ti}, \mu_{Te})$.

3.2. Coakley Turbulence Model

The [11] model is a $k^{1/2}$-ω one. The turbulent Reynolds number is defined as

$$R = \sqrt{k}N/\nu_M. \tag{31}$$

The production term of turbulent kinetic energy is given by

$$P = \left[\left(\frac{\partial u}{\partial y} + \frac{\partial v}{\partial x}\right)\frac{\partial u}{\partial y} + \left(\frac{\partial u}{\partial z} + \frac{\partial w}{\partial x}\right)\frac{\partial w}{\partial x} + \left(\frac{\partial w}{\partial y} + \frac{\partial v}{\partial z}\right)\frac{\partial v}{\partial z}\right] \Big/ Re. \tag{32}$$

The function χ is defined as

$$\chi = \sqrt{\frac{C_\mu P}{\omega^2} - 1}. \tag{33}$$

The damping function is given by

$$D = \frac{1 - e^{-\alpha R}}{1 + \beta\chi}. \tag{34}$$

The turbulent viscosity is defined by

$$\mu_T = Re\, C_\mu D\rho k/\omega, \tag{35}$$

with: C_μ a constant to be defined.

To the [11] model, the G_k and G_ω terms have the following expressions:

$$G_k = -P_k - D_k \quad \text{and} \quad G_\omega = -P_\omega - D_\omega, \tag{36}$$

where:

$$P_k = \left(\frac{0.5C_\mu DP}{\omega^2}\right)\rho\omega\sqrt{k}/Re;\; D_k = 0.5\left[-\frac{2}{3}\left(\frac{\partial u}{\partial x} + \frac{\partial v}{\partial y}\right)\Big/\omega - 1\right]\rho\omega\sqrt{k}/Re; \tag{37}$$

$$P_\omega = \left(C_1 C_\mu P/\omega^2\right)\rho\omega^2/Re;\; D_\omega = \left[-\frac{2}{3}C_1\left(\frac{\partial u}{\partial x} + \frac{\partial v}{\partial y}\right)\Big/\omega - C_2\right]\rho\omega^2/Re, \tag{38}$$

where $C_1 = 0.405D + 0.045$. The closure coefficients adopted for the [11] model are: $\sigma_k = 1.0$; $\sigma_\omega = 1.3$; $C_\mu = 0.09$; $C_2 = 0.92$; $\beta = 0.5$; $\alpha = 0.0065$; Prd_L = 0.72; Prd_T = 0.9.

3.3. Wilcox Turbulence Model

In the [12] turbulence model, s = ω. The turbulent viscosity is expressed in terms of k and ω as:

$$\mu_T = Re\,\rho k/\omega. \tag{39}$$

In this model, the quantities σ_k and σ_ω have the values $1/\sigma^*$ and $1/\sigma$, respectively, where σ^* and σ are model constants.

To the [12] model, the G_k and G_ω terms have the following expressions:

$$G_k = -P_k + D_k \quad \text{and} \quad G_\omega = -P_\omega + D_\omega, \tag{40}$$

where:

$$P_k = \mu_T\left[\left(\frac{\partial u}{\partial y} + \frac{\partial v}{\partial x}\right)\frac{\partial u}{\partial y} + \left(\frac{\partial u}{\partial z} + \frac{\partial w}{\partial x}\right)\frac{\partial w}{\partial x} + \left(\frac{\partial v}{\partial z} + \frac{\partial w}{\partial y}\right)\frac{\partial v}{\partial z}\right] \Big/ Re; \tag{41}$$

$$D_k = \beta^*\rho k\,\omega/Re; \tag{42}$$

$$P_\omega = \left(\frac{\alpha\omega}{k}\right)P_k \quad \text{and} \quad D_\omega = \beta\rho\,\omega^2/Re, \tag{43}$$

where the closure coefficients adopted for the [12] model are: $\beta^* = 0.09$; $\beta = 3/40$; $\sigma^* = 0.5$; $\sigma = 0.5$; $\alpha = 5/9$; Prd_L = 0.72; Prd_T = 0.9.

3.4. Barth and Baldwin Turbulence Model

In this one-equation model, the partial differential equation considered is described as:

$$\frac{D(\nu R_T)}{Dt} = -(c_{\varepsilon 2} f_2 - c_{\varepsilon 1})\sqrt{\nu R_T P} - \left(\nu + \frac{\nu_T}{\sigma_\varepsilon}\right)\left(\frac{\partial^2 \nu R_T}{\partial x^2} + \frac{\partial^2 \nu R_T}{\partial y^2} + \frac{\partial^2 \nu R_T}{\partial z^2}\right) - \left(\frac{1}{\sigma_\varepsilon}\right)\left(\frac{\partial \nu}{\partial x}\frac{\partial \nu R_T}{\partial x} + \frac{\partial \nu}{\partial y}\frac{\partial \nu R_T}{\partial y} + \frac{\partial \nu}{\partial z}\frac{\partial \nu R_T}{\partial z}\right). \quad (44)$$

The terms n this equation are modeled as follows. The wall tension is defined by Eq. (16). The turbulent viscosity is defined as:

$$\mu_T = \mathrm{Re}\, C_\mu \nu R_T D_1 D_2 , \quad (45)$$

where:

$$D_1 = 1 - e^{-N^+/A^+} \quad \text{and} \quad D_2 = 1 - e^{-N^+/A_2^+} ; \quad (46)$$

$$N^+ = \sqrt{\mathrm{Re}\, u_T}\, N/\nu_w . \quad (47)$$

In relation to Eq. (44), the energy term is described by:

$$P = \left[\tau_{xy}\frac{\partial u}{\partial y} - \frac{2}{3}\nu_T\left(\frac{\partial u}{\partial x} + \frac{\partial v}{\partial y} + \frac{\partial w}{\partial z}\right)^2\right]\Big/\mathrm{Re} + \left[\tau_{xz}\frac{\partial u}{\partial z} - \frac{2}{3}\nu_T\left(\frac{\partial u}{\partial x} + \frac{\partial v}{\partial y} + \frac{\partial w}{\partial z}\right)^2\right]\Big/\mathrm{Re} , \quad (48)$$

where:

$$\tau_{xy} = \nu_T\left(\frac{\partial u}{\partial y} + \frac{\partial v}{\partial x}\right) \quad \text{and} \quad \tau_{xz} = \nu_T\left(\frac{\partial u}{\partial z} + \frac{\partial w}{\partial x}\right). \quad (49)$$

The parameter f_2 is defined as:

$$f_2 = \frac{c_{\varepsilon 1}}{c_{\varepsilon 2}} + \left(1 - \frac{c_{\varepsilon 1}}{c_{\varepsilon 2}}\right)\left(\frac{1}{\kappa N^+} + D_1 D_2\right)\left(\sqrt{D_1 D_2} + \frac{N^+}{\sqrt{D_1 D_2}}\right)\left(\frac{1}{A^+}e^{-N^+/A^+}D_2 + \frac{1}{A_2^+}e^{-N^+/A_2^+}D_1\right). \quad (50)$$

It is important to remember that due to the present nondimensionalization, the second and the third terms of the RHS of Eq. (44) are divided by the Reynolds number.

The model constants have the following values: $\kappa = 0.41$, $c_{\varepsilon 1} = 1.2$, $c_{\varepsilon 2} = 2.0$, $C_\mu = 0.09$, $A^+ = 26.0$, $A_2^+ = 10.0$, and $\sigma_\varepsilon = \dfrac{\kappa^2}{(c_{\varepsilon 2} - c_{\varepsilon 1})\sqrt{C_\mu}}$.

4. Initial and Boundary Conditions

The initial and boundary conditions to the [10] turbulence model are the same of those found in [19-20]. For the $k^{1/2}$-ω and k-ω models, one has:

4.1. Initial Condition

Freestream values, at all grid cells, are adopted for all flow properties as initial condition, as suggested by [21-22]. Therefore, the vector of conserved variables is defined as:

$$Q_{i,j,k} = \left\{1 \quad M_\infty \cos\alpha \quad M_\infty \sin\alpha\cos\theta \quad M_\infty \sin\alpha\sin\theta \quad \frac{1}{\gamma(\gamma-1)} + 0.5M_\infty^2 \quad t_\infty \quad s_\infty\right\}^T , \quad (51)$$

where t_∞ is the freestream turbulent kinetic energy and s_∞ is the freestream turbulent vorticity or the squared of this value. These parameters assume the following values as using the [11] model: $t_\infty = 1.0\text{x}10^{-3}$ and $s_\infty = (10u_\infty/l_{REF})$, and as using the [12] model: $t_\infty = 1.0\text{x}10^{-6}$ and $s_\infty = (10u_\infty/l_{REF})$, with u_∞ the freestream u Cartesian component and l_{REF} a characteristic length, the same adopted in the definition of the Reynolds number.

For the one-equation model:

4.2. Initial Condition

$$Q_{i,j,k} = \left\{1 \quad M_\infty \cos\alpha \quad M_\infty \sin\alpha\cos\theta \quad M_\infty \sin\alpha\sin\theta \quad \frac{1}{\gamma(\gamma-1)} + 0.5M_\infty^2 \quad (\nu R_T)_\infty\right\}^T , \text{ with } (\nu R_T)_\infty = 0.5\nu . \quad (52)$$

4.3. Boundary Conditions

For the $k^{1/2}$-ω and k-ω models:

The boundary conditions are basically of four types: solid wall, entrance, exit and far field. These conditions are implemented with the help of ghost cells.

(1) Wall condition: At a solid boundary the non-slip condition is enforced. Therefore, the tangent velocity component of the ghost volume at wall has the same magnitude as the respective velocity component of its real neighbor cell, but opposite signal. In the same way, the normal velocity component of the ghost volume at wall is equal in value, but opposite in signal, to the respective velocity component of its real neighbor cell.

The normal pressure gradient of the fluid at the wall is assumed to be equal to zero in a boundary-layer like condition. The same hypothesis is applied for the normal temperature gradient at the wall, assuming an adiabatic wall. The normal gradient of the turbulence kinetic energy at the wall is also assumed to be equal to zero.

From the above considerations, density and pressure are extrapolated from the respective values of its real neighbor volume (zero order extrapolation). The total energy is obtained by the state equation for a perfect gas. The turbulent kinetic energy and the turbulent vorticity at the ghost volumes are determined by the following expressions:

$$k_{ghost} = 0.0 \quad \text{and} \quad \omega = \left[\left(38/3\nu_M\right)/\left(\beta d_n^2\right)\right], \tag{53}$$

where β assumes the value 3/40 and d_n is the distance of the first cell to the wall.

(2) Entrance condition:

(2.1) Subsonic flow: Six properties are specified and one extrapolated. This approach is based on information propagation analysis along characteristic directions in the calculation domain ([22]). In other words, for subsonic flow, six characteristic propagate information pointing into the computational domain. Thus six flow properties must be fixed at the inlet plane. Just one characteristic line allows information to travel upstream. So, one flow variable must be extrapolated from the grid interior to the inlet boundary. The pressure was the extrapolated variable from the real neighbor volumes, for the studied problem. Density and velocity components adopted values of freestream flow. The turbulence kinetic energy and the vorticity were fixed with the values of the initial condition. The turbulence kinetic energy receives the value 0.01 of K. The total energy is determined by the state equation of a perfect gas.

(2.2) Supersonic flow: In this case no information travels upstream; therefore all variables are fixed with their of freestream values.

(3) Exit condition:

(3.1) Subsonic flow: Six characteristic propagate information outward the computational domain. Hence, the associated variables should be extrapolated from interior information. The characteristic direction associated to the "(q_{normal}-a)" velocity should be specified because it points inward to the computational domain ([22]). In this case, the ghost volume pressure is specified from its initial value. Density, velocity components, the turbulence kinetic energy, and the vorticity are extrapolated. The total energy is obtained from the state equation of a perfect gas.

(3.2) Supersonic flow: All variables are extrapolated from interior grid cells, as no flow information can make its way upstream. In other words, nothing can be fixed.

(4) Far field condition: The mean flow kinetic energy is assumed to be $K = 0.5u^2$ and the turbulence kinetic energy at the far field adopts the value $k_{ff} = 0.01K$, or 1% of K. The turbulence vorticity is determined by its freestream value.

For the one-equation model:

4.4. Boundary Conditions

The boundary conditions are basically of three types: solid wall, entrance and exit. For the wall condition, one adopts $(\nu R_T)_w = 0.0$. For the entrance condition, it is assumed 0.5ν or zero-order extrapolation if the flow is pointing into the computational field or pointing out of the computational field, respectively. For the exit condition, one adopts zero-order extrapolation.

5. Results

Tests were performed in an INTEL Core i7 processor of 2.10GHz and 8.0Gbytes of RAM microcomputer in a Windows 7.0 environment. Three orders of reduction of the maximum residual in the field were considered to obtain a converged solution. The residual was defined as the value of the discretized conservation equation. The entrance or attack angle was adopted equal to zero, as well the longitudinal angle. The ratio of specific heats, γ, assumed the value 1.4.

Figure 1 shows the blunt body configuration, whereas Fig. 2 shows the blunt body mesh. A mesh of 53x50x10 points or composed of 22,932 hexahedron cells and 26,500 nodes was generated, employing an exponential stretching of 5.0% in the η direction.

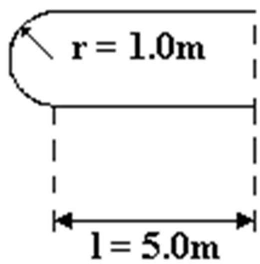

Figure 1. *Blunt body configuration.*

The initial data of the simulations is described in Tab. 1.

Table 1. *Initial Conditions.*

M_∞	α	θ	Altitude	L_∞	Re
3.0	0.0°	0.0°	40,000m	2.0m	$4.75\text{x}10^5$

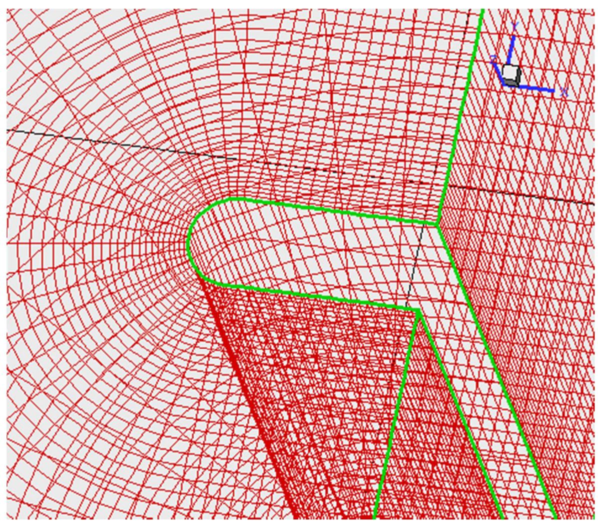

Figure 2. *Blunt body mesh.*

5.1. Granville Results

Figures 3 and 4 present the pressure contours obtained by the [2] and [3] schemes, respectively, as using the [10] turbulence model in three-dimensions. Both fields are homogeneous and the pressure contours generated by the [2] scheme is more strength than the respective one generated by the [3] scheme.

Figures 5 and 6 show the Mach number contours obtained by the [2] and [3] numerical schemes, respectively, as using the [10] turbulence model. Both Mach number fields are free of pre-shock oscillations and are homogeneous. The differences between these fields are only in qualitative terms. It is possible to see that the [2] solution develops a region of low Mach number contours close to the wall, resulting from the boundary layer formation. On the contrary, the [3] solution does not yields this region.

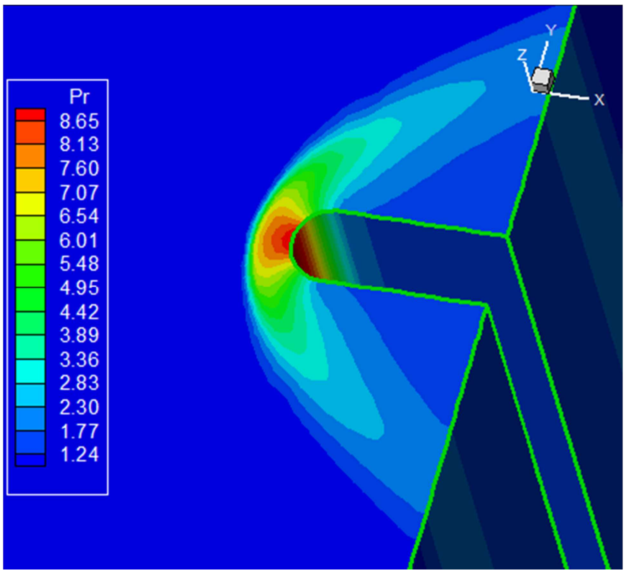

Figure 3. *Pressure contours ([2]).*

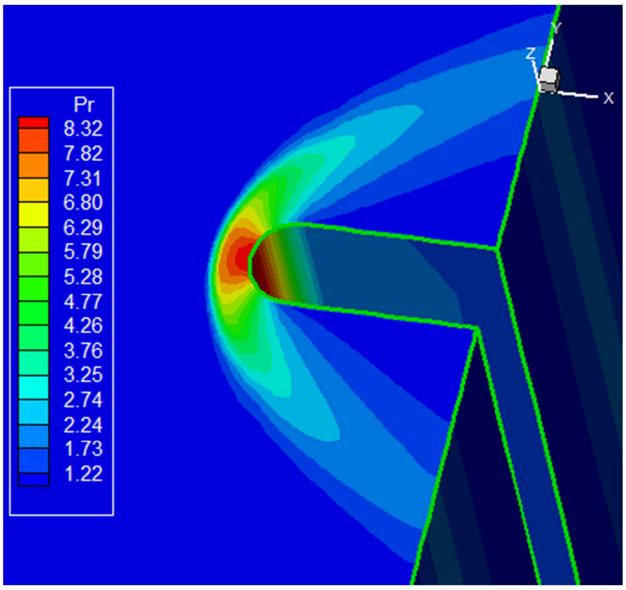

Figure 4. *Pressure contours ([3]).*

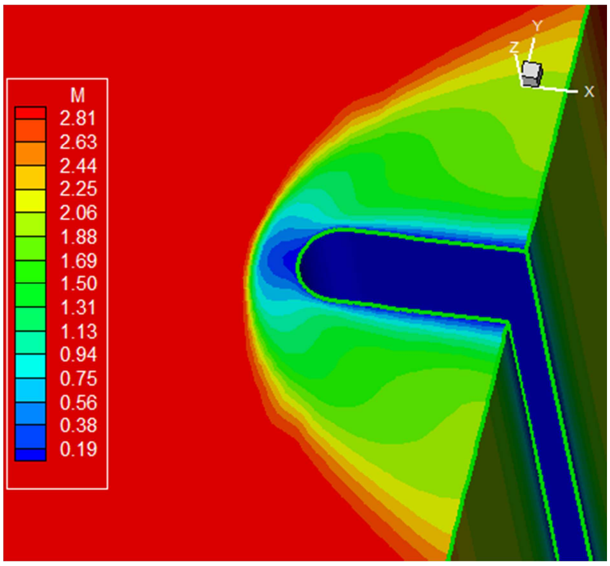

Figure 5. *Mach number contours ([2]).*

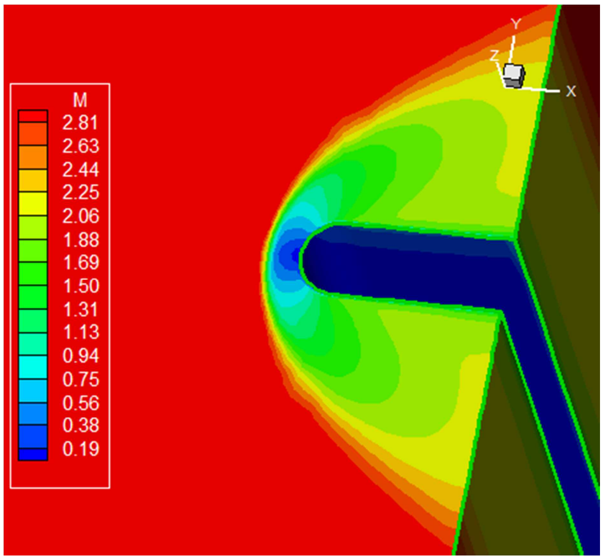

Figure 6. *Mach number contours ([3]).*

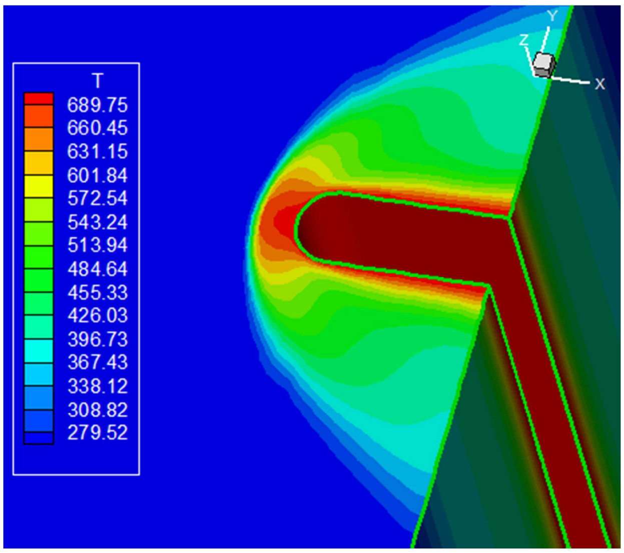

Figure 7. *Temperature contours ([2]).*

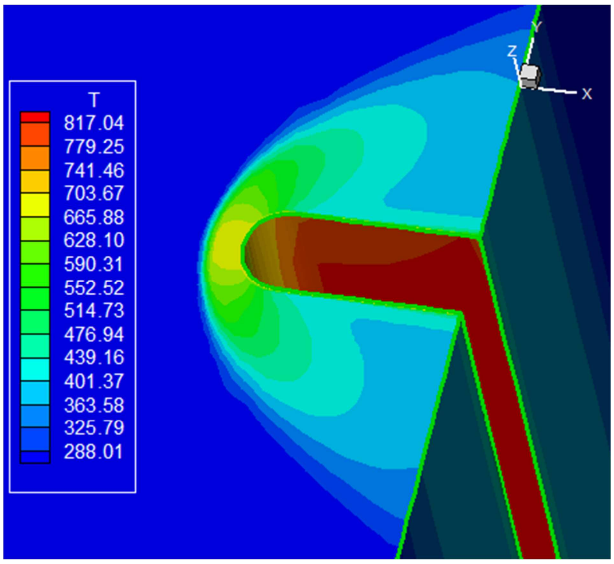

Figure 8. *Temperature contours ([3]).*

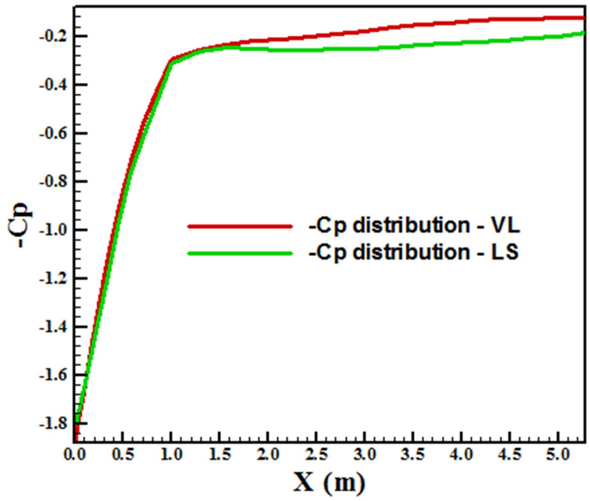

Figure 9. *Cp distributions.*

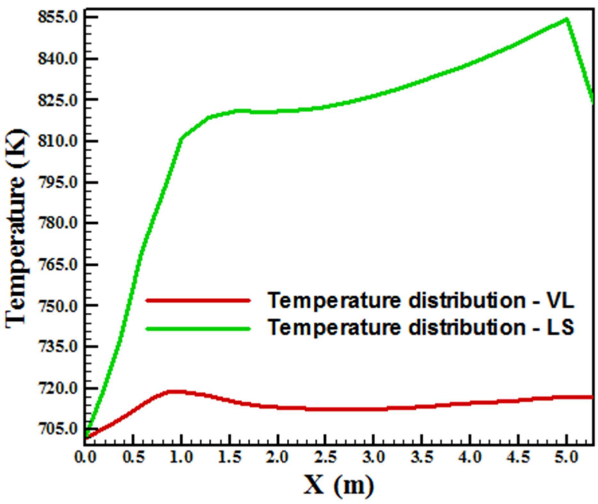

Figure 10. *Wall temperature distributions.*

Figures 7 and 8 exhibit the translational temperature contours obtained by the [2] and [3] schemes, respectively, as using the [10] turbulence model. The temperature contours generated by the [3] scheme is more intense than the respective one of the [2] scheme. However, the [2] solution presents a zone of high dissipation close to the wall, whereas the [3] scheme does not. There are qualitative differences between the two solutions, but both present homogeneous contours, without oscillations. Some problems with the [3] solution in the k = constant planes are observed, which prejudices the solution repetition in these planes. The [2] solution does not present such problems.

Figure 9 exhibits the -Cp distributions generated by the [2] and [3] schemes as using the [10] turbulence model. The -Cp plateau of the [2] scheme is higher than the -Cp plateau of the [3] scheme. The -Cp peak at the body nose is the same for both schemes. Figure 10 presents the wall temperature distributions generated by the [2] and [3] numerical schemes as using the [10] turbulence model. The temperature distribution is smoother for the [2] scheme. The temperature distribution of the [3] scheme is more intense than the respective one of the [2] scheme. The maximum temperature obtained by the [2] scheme is about 720.0 K, whereas that obtained by the [3] scheme is about 855.0 K.

5.2. Coakley Results

Figure 11 and 12 present the pressure contours obtained by the [2] and [3] schemes, respectively, as using the [11] turbulence model. Again, the pressure contours generated by the [2] scheme is more strength than the one generated by the [3] scheme. Good homogeneity is observed in both solutions.

Figures 13 and 14 show the Mach number contours generated by the [2] and [3] schemes, respectively, as using the [11] turbulence model. Both solutions are identical in quantitative terms, only being different in qualitative terms. The subsonic region close to the body wall is again observed in the [2] solution. The subsonic region at the body nose is observed, as resulting from the shock slowdown. No pre-shock oscillations are observed in both solutions.

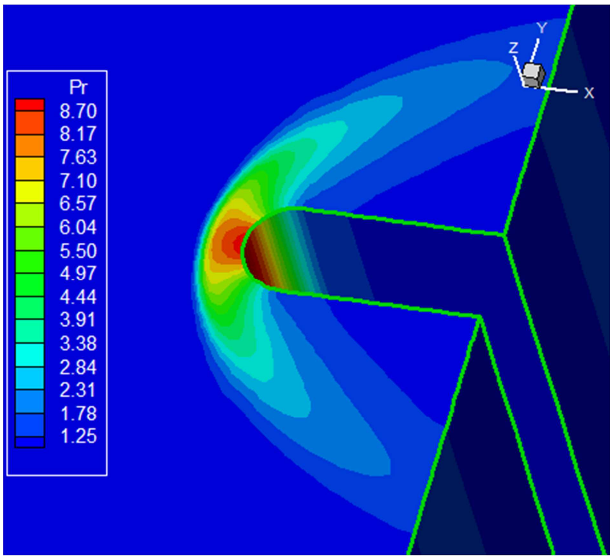

Figure 11. *Pressure contours ([2]).*

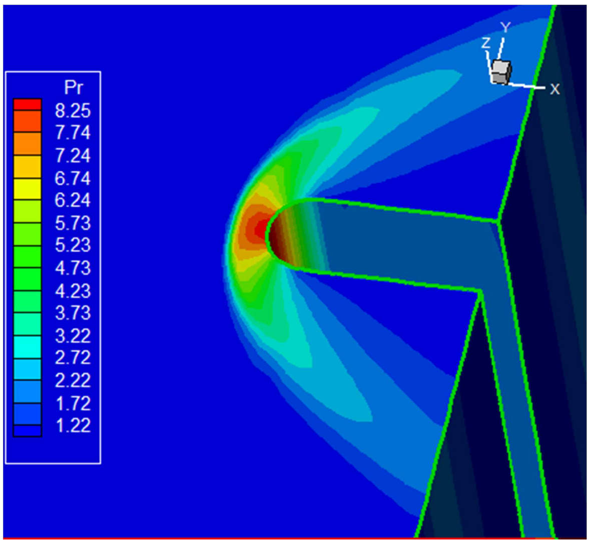

Figure 12. *Pressure contours ([3]).*

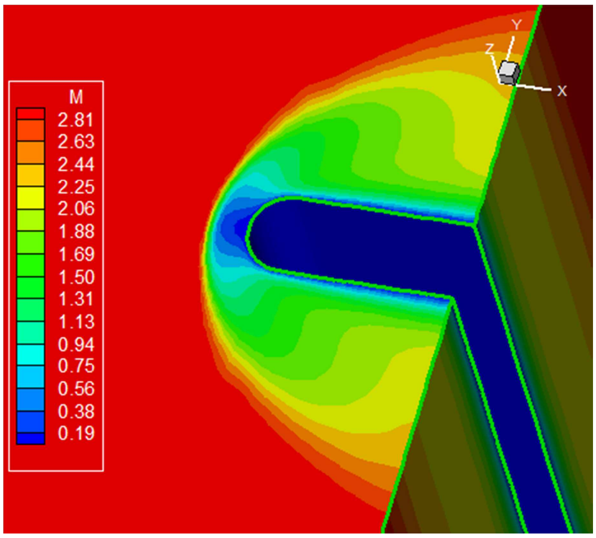

Figure 13. *Mach number contours ([2]).*

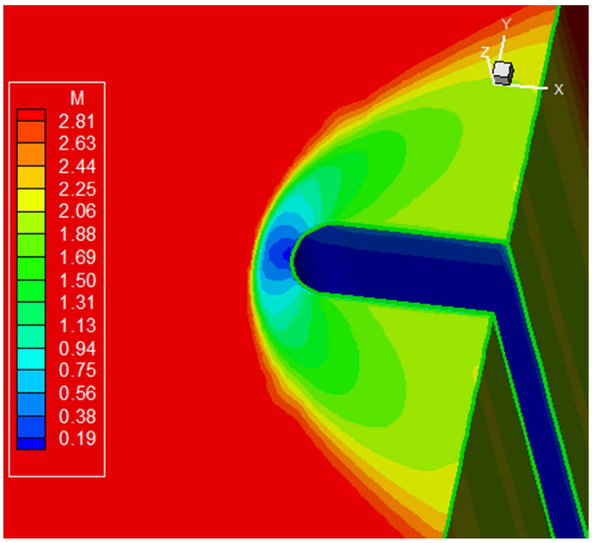

Figure 14. *Mach number contours ([3]).*

Figures 15 and 16 exhibit the translational temperature contours obtained by the [2] and [3] schemes, respectively, as using the [11] turbulence model. The [2] solution presents higher temperatures in the field than the [3] solution.

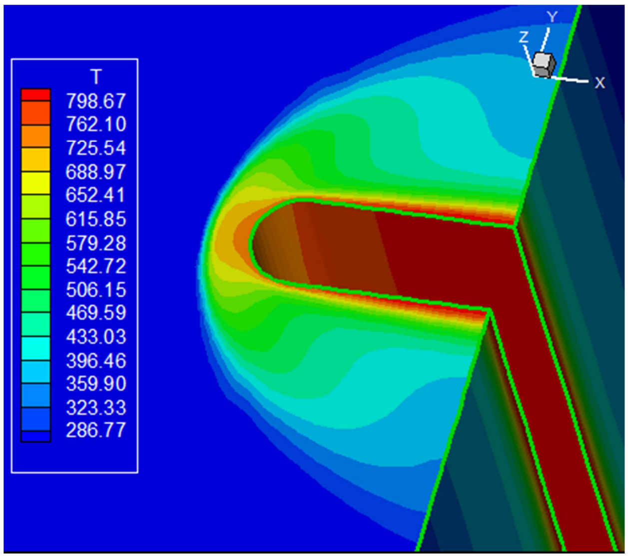

Figure 15. *Temperature contours ([2]).*

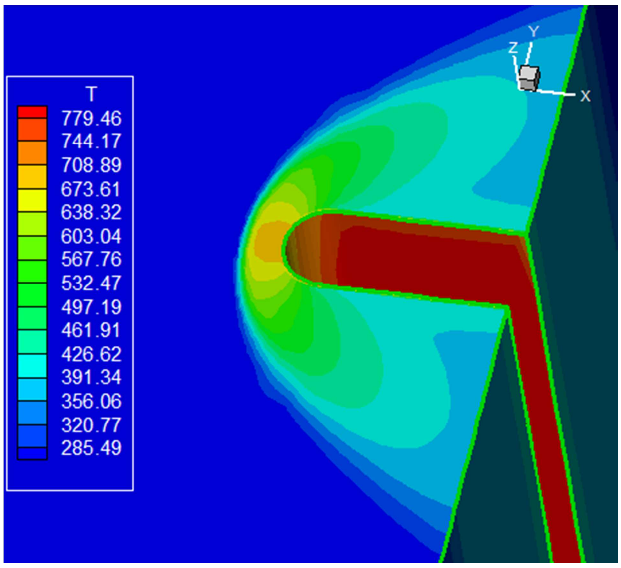

Figure 16. *Temperature contours ([3]).*

Moreover, the [2] solution presents a zone of high dissipation close to body wall, resulting from intense heat energy exchange and boundary layer interaction.

Figure 17 presents the –Cp distribution generated by the [2] and [3] schemes as using the [11] turbulence model. As can be seen the –Cp plateau obtained by the [2] scheme is higher than the respective one of the [3] scheme. The –Cp peak is approximately the same for both solutions. Figure 18 shows the wall translational temperature distributions originated by the [2] and [3] schemes as using the [11] turbulence model. The [2] temperature distribution is smoother than the [3] one. The temperature at the body nose is higher in the [2] solution. The [2] temperature distribution increases along the body. The [2] temperature at the body nose is 48.0 K higher than the [3] temperature one.

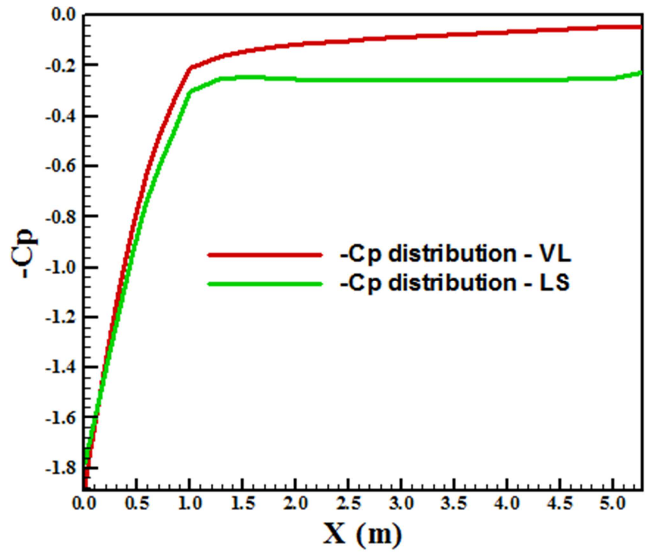

Figure 17. Cp distributions.

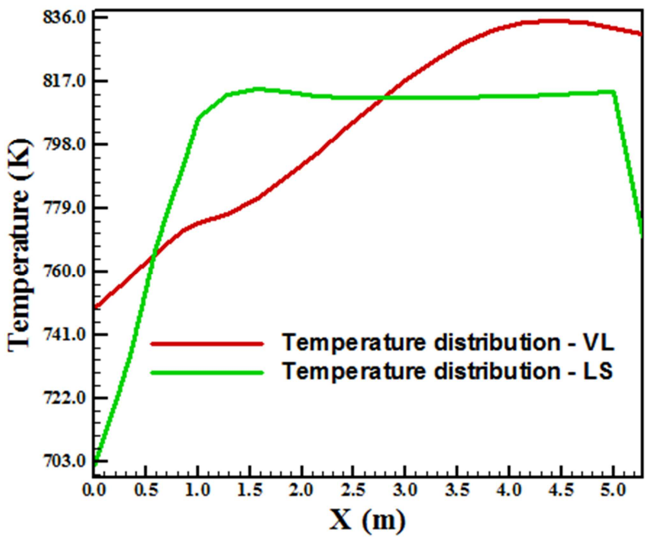

Figure 18. Wall temperature distributions.

5.3. Wilcox Results

Figures 19 and 20 exhibit the pressure contours generated by the [2] and [3] schemes, respectively, as using the [12] turbulence model. The pressure field generated by the [2] scheme is higher than the respective one generated by the [3] scheme. Both pressure fields present good homogeneity properties. Figures 21 and 22 show the Mach number contours obtained by the [2] and [3] schemes, respectively, as using the [12] turbulence model. The Mach number field generated by the [2] scheme is more intense than the respective one of the [3] scheme. Particularly, the zone of low Mach number close to the body wall is only perceptible in the [2] solution. The region of subsonic Mach number at the body nose is well captured by both schemes. No pre-shock oscillations are observed in both figures. The shock wave is well captured in both solutions.

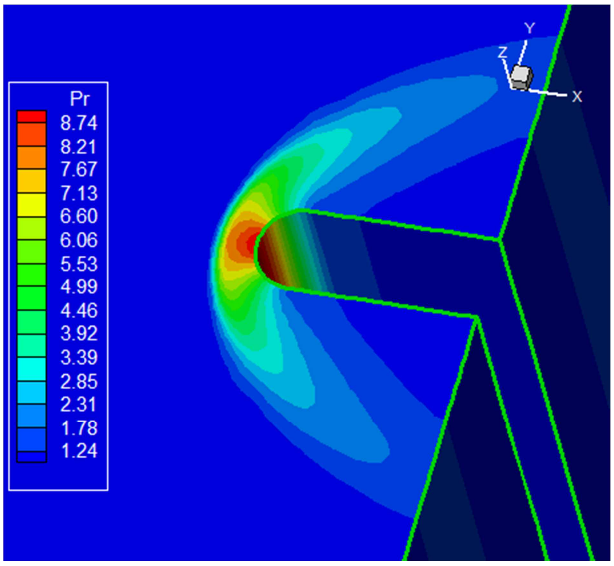

Figure 19. Pressure contours ([2]).

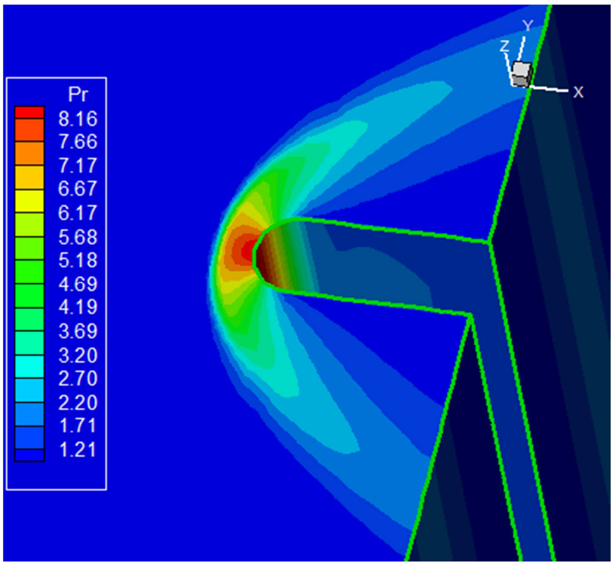

Figure 20. Pressure contours ([3]).

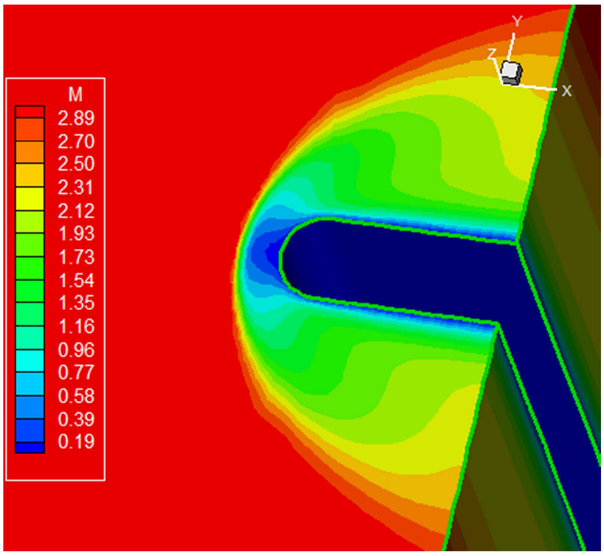

Figure 21. Mach number contours ([2]).

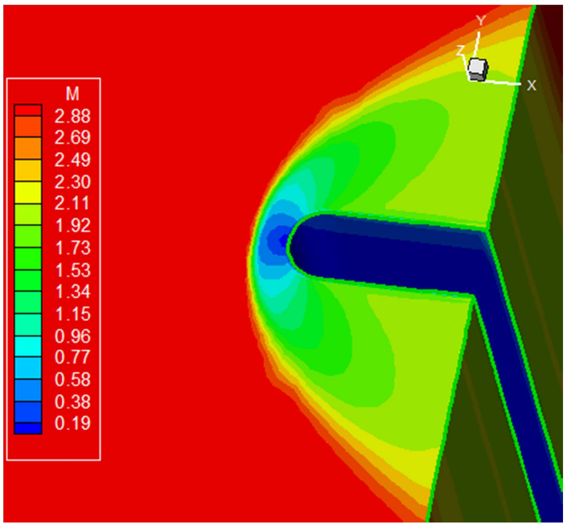

Figure 22. *Mach number contours ([3]).*

Good homogeneous properties are observed in both figures. The zone of intense energy exchange, close to the body wall, is observed in the [2] solution. Moreover, the zone of intense temperature is slightly observed at the body nose in both solutions, as expected. Good symmetry properties are noted in both solutions.

Figures 23 and 24 exhibit the translational temperature contours obtained by the [2] and [3] schemes, respectively, as using the [12] turbulence model. The temperature field generated by the [2] scheme is again more intense than the respective one of the [3] scheme.

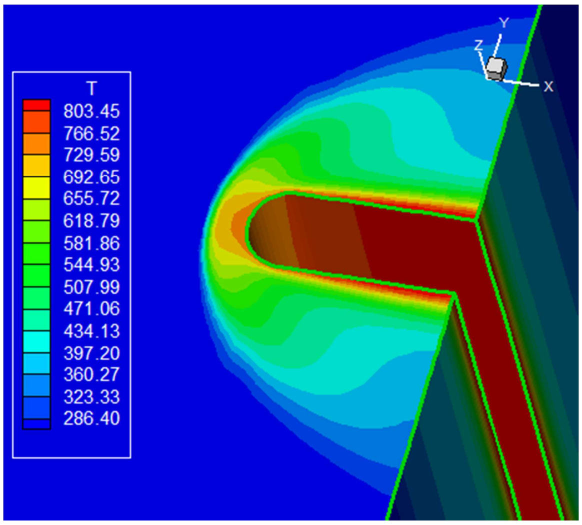

Figure 23. *Temperature contours ([2]).*

Figure 25 presents the –Cp distribution obtained by the [2] and [3] schemes as using the [12] turbulence model. In accordance to the observed in the ultimate solutions, the [2] scheme presents higher –Cp plateau than the [3] scheme; Moreover, both solutions present the same –Cp peak, at the body nose. Figure 26 shows the wall temperature distributions obtained by the [2] and [3] schemes as using the [12] turbulence model. Both solutions present different temperature peaks at the leading edge, the difference around 45.0 K. Again the [2] solution presents an increase of the temperature along the body, whereas the [3] solution suffers a reduction along the body. The maximum temperature reached by the [2] scheme is about 840.0 K, whereas by the [3] scheme is 804.0 K.

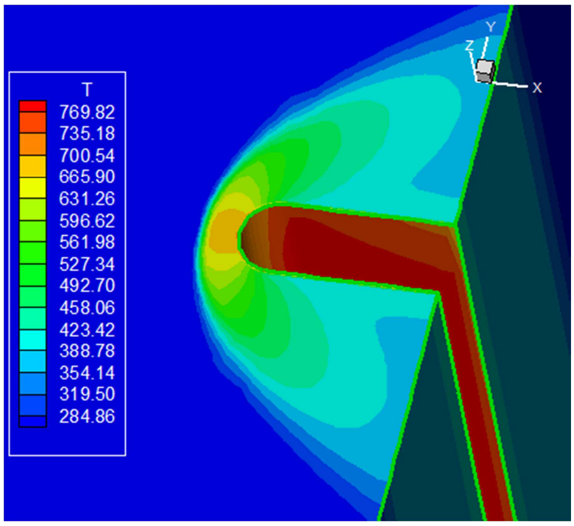

Figure 24. *Temperature contours ([3]).*

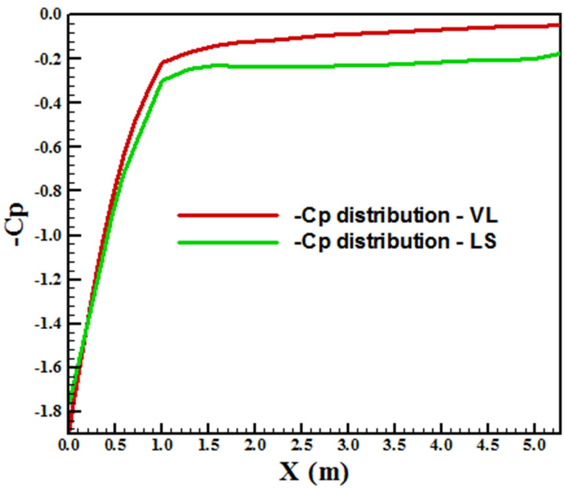

Figure 25. *Cp distributions.*

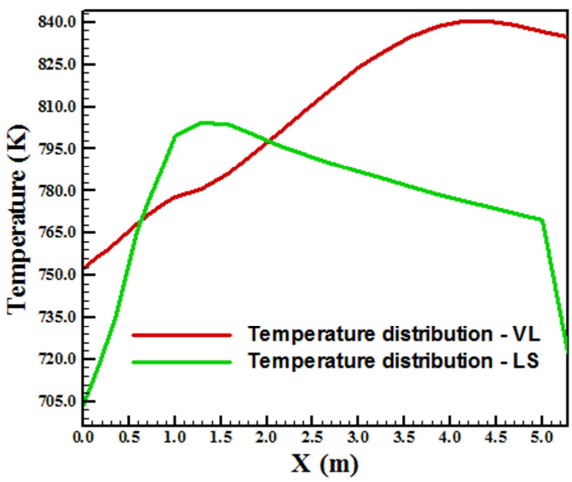

Figure 26. *Wall temperature distributions.*

5.4. Baldwin and Barth Results

Figures 27 and 28 show the pressure contours obtained by the [2] and [3] schemes, respectively, as using the [13] turbulence model. As can be observed, the [2] scheme predicts again more severe pressure field than the [3] scheme. The shock is well capture and good symmetry characteristics are noted. Good homogeneity in both solutions is also observed.

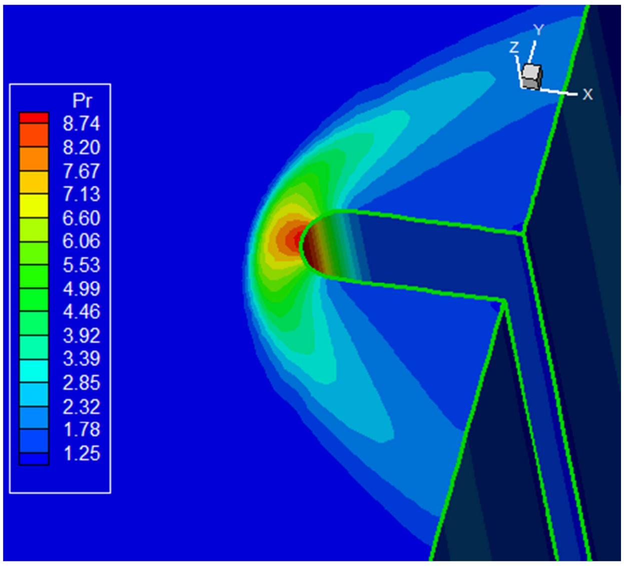

Figure 27. *Pressure contours ([2]).*

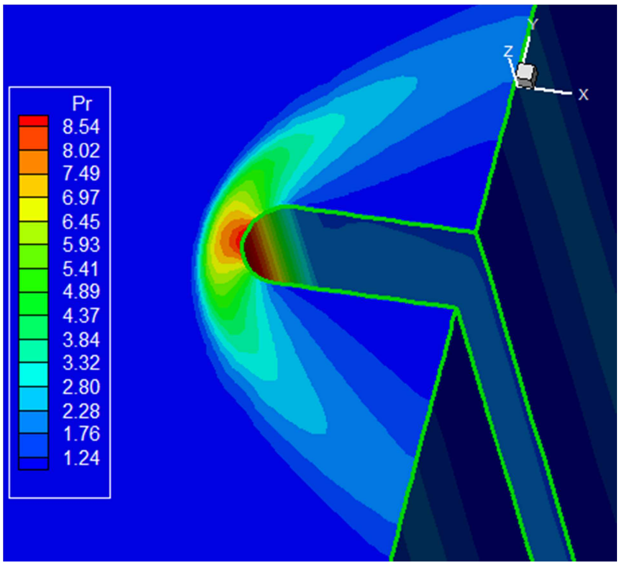

Figure 28. *Pressure contours ([3]).*

Figures 29 and 30 present the Mach number contours generated by the [2] and [3] schemes, respectively, as using the [13] turbulence model. Good symmetry properties are observed, without pre-shock oscillations. Good homogeneity properties are noted. The Mach number fields are identical in quantitative terms, although in qualitative terms some discrepancies are observed. The zone of low Mach number close to the body wall is only noted in the [2] solution.

Figures 31 and 32 show the translational temperature contours obtained by the [2] and [3] schemes, respectively, as using the [13] turbulence model. As can be observed, the [3] temperature field is more intense than the [2] temperature field. The zone of intense energy exchange observed close to the body wall is only captured by the [2] scheme. Moreover, the intense temperature region at the body nose is again only observed in the [2] solution, being more discrete in the [3] case. Good symmetry properties are observed in both figures.

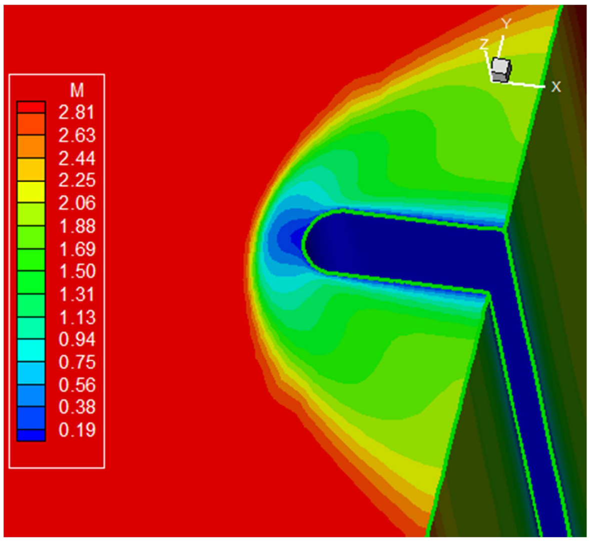

Figure 29. *Mach number contours ([2]).*

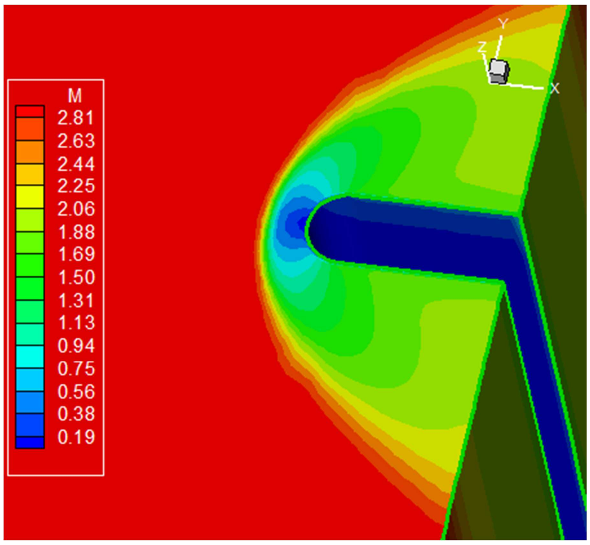

Figure 30. *Mach number contours ([3]).*

Figure 33 exhibits the –Cp distributions at the wall obtained by the [2] and [3] schemes as using the [13] turbulence model. As observed in all solutions, the [2] scheme presents again a pressure plateau higher than the [3] scheme does, although both –Cp peaks at the body nose are approximately the same. Figure 34 shows the temperature distributions at wall generated by the [2] and [3] schemes as using the [13] turbulence model. The [2] temperature distributions is smoother than the [3] one. The [2] temperature distribution keeps approximately the same behavior along the body length, whereas the [3] temperature distribution increases and close to the body end reduces its value. The temperature values at the body end are approximately 700.0 K to the [2] scheme and 760.0 K to the [3] scheme. The maximum temperature values are 712.0 K to the [2] scheme and 800.0 K to the [3] scheme.

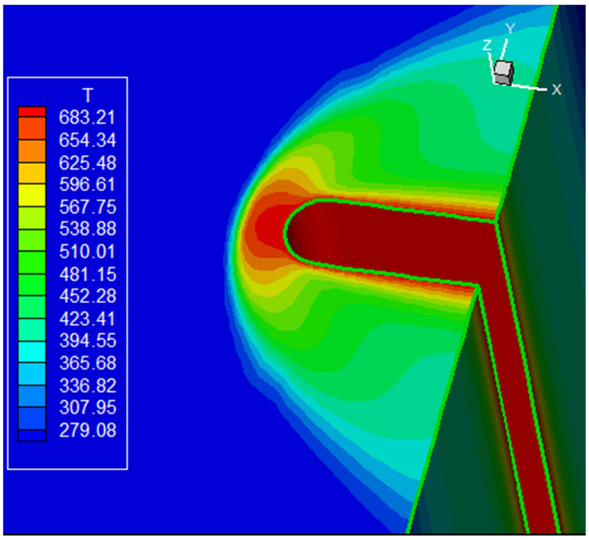

Figure 31. *Temperature contours ([2]).*

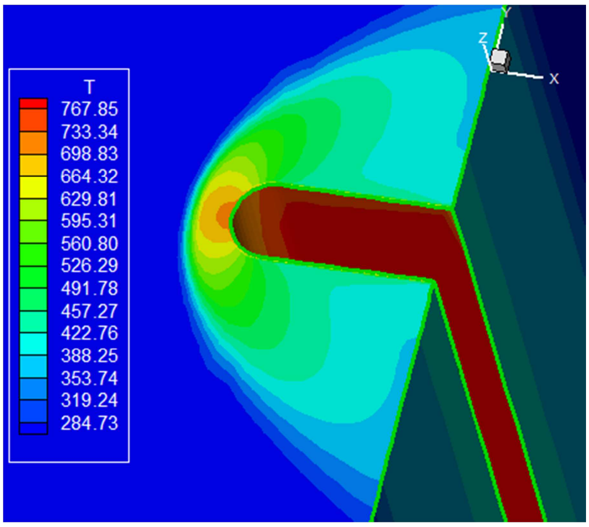

Figure 32. *Temperature contours ([3]).*

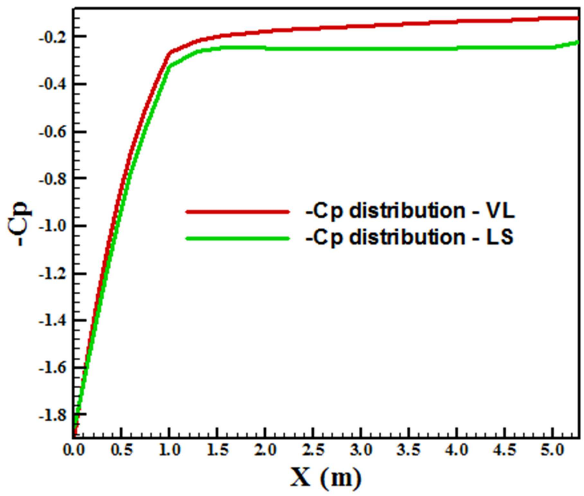

Figure 33. *Cp distributions.*

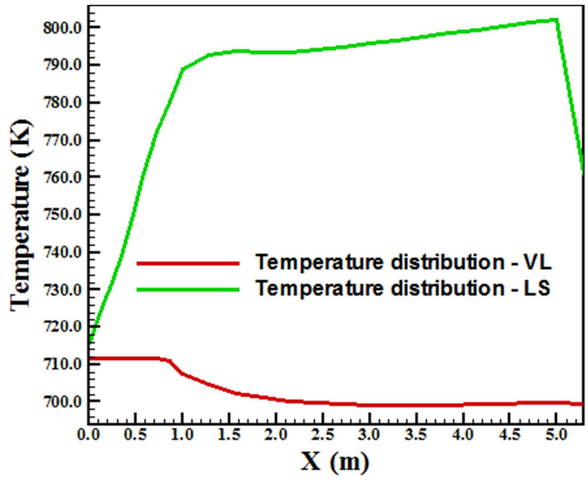

Figure 34. *Wall temperature distributions.*

5.5. Quantitative Analysis

A possibility to quantitative comparison of the turbulent cases is the determination of the stagnation pressure ahead of the configuration. [23] presents a table of normal shock wave properties in its B Appendix. This table permits the determination of some shock wave properties as function of the freestream Mach number. In front of the blunt body configuration, the shock wave presents a normal shock behavior, which permits the determination of the stagnation pressure, behind the shock wave, from the tables encountered in [23]. So it is possible to determine the ratio pr_0/pr_∞ from [23], where pr_0 is the stagnation pressure in front of the configuration and pr_∞ is the freestream pressure (equals to $1/\gamma$ to the present dimensionless).

Hence, to this problem, $M_\infty = 3.0$ corresponds to $pr_0/pr_\infty = 12.06$ and remembering that $pr_\infty = 0.714$, it is possible to conclude that $pr_0 = 8.61$. Values of the stagnation pressure to the turbulent cases and respective percentage errors are shown in Tab. 2. They are obtained from Figures 3, 4, 11, 12, 19, 20, 27 and 28. As can be observed, the [2] scheme using the [10] turbulence model has presented the best result, with a percentage error of 0.46%. It is important to observe that, although first order schemes were used, the percentage relative errors were inferior to 5.50%.

Finally, Table 3 exhibits the computational data of the present simulations. It can be noted that the most efficient is the [2] scheme using the [12] turbulence model. All schemes used a CFL number of 0.10, not necessarily being the maximum CFL number of each one.

Table 2. *Values of the stagnation pressure and respective percentage errors.*

Model:	Scheme:	pr_0:	Error (%):
[10]	[2]	8.65	0.46
	[3]	8.32	3.37
[11]	[2]	8.70	1.05
	[3]	8.25	4.18
[12]	[2]	8.74	1.51
	[3]	8.16	5.23
[13]	[2]	8.74	1.51
	[3]	8.54	0.81

Table 3. *Computational data.*

Model:	Scheme:	CFL:	Iterations:
[10]	[2]	0.10	2,704
	[3]	0.10	2,278
[11]	[2]	0.10	746
	[3]	0.10	3,099
[12]	[2]	0.10	729
	[3]	0.10	3,200
[13]	[2]	0.10	2,572
	[3]	0.10	2,429

As final conclusion of this study, the [10] turbulence model was the best when comparing these four turbulence models: [10], [11], [12] and [13]. In a next paper, the present author will study more four different turbulent models to this same problem trying to identify the best of each group of four and to perform a final analysis to found the best one.

6. Conclusions

In the present work, the [2-3] flux vector splitting schemes are implemented, on a finite-volume context. The three-dimensional Favre-averaged Navier-Stokes equations are solved using an upwind discretization on a structured mesh. The [10] algebraic model, the [11] and [12] $k^{1/2}$-ω and k-ω two-equation models, respectively, and the [13] one-equation model are used in order to close the problem. The physical problem under study is the supersonic flow around a blunt body configuration. The implemented schemes are first-order accurate in space. The time integration uses a Runge-Kutta method of five stages and is second-order accurate. The algorithms are accelerated to the steady state solution using a spatially variable time step. This technique has proved excellent gains in terms of convergence rate as reported in [14-15].

The results have demonstrated that the [2] scheme using the [10] turbulence model has yielded the best value of the stagnation pressure at the blunt body nose and is the best choice for this study. The most efficient scheme has been the [2] one using the [12] turbulence model.

Acknowledgment

The author thanks the CAPES by the financial support conceded under the form of a scholarship. He also acknowledges the infrastructure of ITA that allowed the realization of this work.

References

[1] P. Kutler, “Computation of Three-Dimensional, Inviscid Supersonic Flows”, *Lecture Notes in Physics*, Vol. 41, 1975, pp. 287-374.

[2] B. Van Leer, “Flux-Vector Splitting for the Euler Equations”, *Proceedings of the 8th International Conference on Numerical Methods in Fluid Dynamics*, E. Krause, Editor, *Lecture Notes in Physics*, Vol. 170, 1982, pp. 507-512, Springer-Verlag, Berlin.

[3] M. Liou, and C. J. Steffen Jr., “A New Flux Splitting Scheme”, *Journal of Computational Physics*, Vol. 107, 1993, pp. 23-39.

[4] E. S. G. Maciel, “Assessment of Several Turbulence Models Applied to Supersonic Flows in Three-Dimensions – Part I”, *Computational and Applied Mathematics Journal*, Vol. 1, Issue 4, 2015, June, pp. 156-173.

[5] E. S. G. Maciel, and N. G. C. R. Fico Jr., “Estudos de Escoamentos Turbulentos Utilizando o Modelo de Baldwin e Lomax e Comparação entre Algoritmos Explícitos e Implícitos”, *Proceedings of the III National Congress of Mechanical Engineering (III CONEM)*, Belém, PA, Brazil, 2004. [CD-ROM]

[6] B. S. Baldwin, and H. Lomax, “Thin Layer Approximation and Algebraic Model for Separated Turbulent Flows”, *AIAA Paper 78-257*, 1978.

[7] R. W. MacCormack, “The Effect of Viscosity in Hypervelocity Impact Cratering”, *AIAA Paper 69-354*, 1969.

[8] T. H. Pulliam, and D. S. Chaussee, “A Diagonal Form of an Implicit Approximate-Factorization Algorithm”, *Journal of Computational Physics*, Vol. 39, 1981, pp. 347-363.

[9] A. Jameson, W. Schmidt, and E. Turkel, “Numerical Solution of the Euler Equations by Finite Volume Methods Using Runge-Kutta Time Stepping Schemes”, *AIAA Paper 81-1259*, 1981.

[10] P. S. Granville, “Baldwin Lomax Factors for Turbulent Boundary Layers in Pressure Gradients”, *AIAA Journal*, Vol. 25, pp. 1624-1627, 1989.

[11] T. J. Coakley, “Turbulence Modeling Methods for the Compressible Navier-Stokes Equations”, *AIAA Paper No. 83-1693*, 1983.

[12] D. C. Wilcox, “Reassessment of the Scale-Determining Equation for Advanced Turbulence Models”, *AIAA Journal*, Vol. 26, November, pp. 1299-1310, 1988.

[13] B. S. Baldwin, and T. J. Barth, “A One-Equation Turbulence Transport Model for High Reynolds Number Wall-Bounded Flows”, AIAA Paper 91-0610, 1991.

[14] E. S. G. Maciel, *Simulations in 2D and 3D Applying Unstructured Algorithms, Euler and Navier-Stokes Equations – Perfect Gas Formulation*. Saarbrücken, Deutschland: Lambert Academic Publishing (LAP), 2015, Ch. 1, pp. 26-47.

[15] E. S. G. Maciel, *Simulations in 2D and 3D Applying Unstructured Algorithms, Euler and Navier-Stokes Equations – Perfect Gas Formulation*. Saarbrücken, Deutschland: Lambert Academic Publishing (LAP), 2015, Ch. 6, pp. 160-181.

[16] R. W. Fox, and A. T. McDonald, *Introdução à Mecânica dos Fluidos*. Ed. Guanabara Koogan, Rio de Janeiro, RJ, Brazil, 632 p, 1988.

[17] E. S. G. Maciel, *Applications of TVD Algorithms in 2D and 3D, Euler and Navier-Stokes Equations in 2D and 3D*. Saarbrücken, Deutschland: Lambert Academic Publishing (LAP), 2015, Ch. 13, pp. 463-466.

[18] D. J. Mavriplis, and A. Jameson, “Multigrid Solution of the Navier-Stokes Equations on Triangular Meshes”, *AIAA Journal*, Vol. 28, No. 8, 1990, pp. 1415-1425.

[19] E. S. G. Maciel, "Comparação entre os Modelos de Turbulência de Cebeci e Smith e de Baldwin e Lomax", *Proceedings of the 5th Spring School of Transition and Turbulence (V EPTT)*, Rio de Janeiro, RJ, Brazil, 2006. [CD-ROM]

[20] E. S. G. Maciel, "Estudo de Escoamentos Turbulentos Utilizando os Modelos de Cebeci e Smith e de Baldwin e Lomax e Comparação entre os Algoritmos de MacCormack e de Jameson e Mavriplis", *Proceedings of the 7th Symposium of Computational Mechanics (VII SIMMEC),* Araxá, MG, Brazil, 2006. [CD-ROM]

[21] A. Jameson, and D. Mavriplis, "Finite Volume Solution of the Two-Dimensional Euler Equationson a Regular Triangular Mesh", *AIAA Journal*, vol. 24, no. 4, pp. 611-618, 1986.

[22] E. S. G. Maciel, "Simulação Numérica de Escoamentos Supersônicos e Hipersônicos Utilizando Técnicas de Dinâmica dos Fluidos Computacional", *Doctoral Thesis*, ITA, CTA, São José dos Campos, SP, Brazil, 2002.

[23] J. D. Anderson Jr., *Fundamentals of Aerodynamics*. McGraw-Hill, Inc., EUA, 4th Edition, 1008p, 2005.